Pore Evolution during Combustion of Distinct Thermally Mature Shales
Insights into Potential In Situ Conversion

Hazra, Bodhisatwa; Chandra, Debanjan; Lahiri, Sivaji; Vishal, Vikram; Sethi, Chinmay; Pandey, Jai Krishna

Pore Evolution during Combustion of Distinct Thermally Mature Shales: Insights into Potential In Situ Conversion

Bodhisatwa Hazra, Debanjan Chandra, Sivaji Lahiri, Vikram Vishal,* Chinmay Sethi, and Jai Krishna Pandey

ACCESS | Metrics & More | Article Recommendations

ABSTRACT: Organic-rich shales are marked by the presence of complex pore structures and extremely low permeabilities, which present challenges while extracting hydrocarbon from them. With the potential negative environmental impacts of hydraulic fracturing, recent research has focused on alternative techniques such as in situ combustion/pyrolysis for enhancing the permeability of shales. In this study, low-temperature combustion was used to evaluate the evolution of pore structures in shales for contrasting thermal maturities and organic matter type from the Raniganj and Bikaner−Nagaur basins of India. The heating temperatures were decided on the basis of the combustion behavior of the samples observed from thermogravimetric analysis (TGA). Results from low-pressure N_2 and CO_2 gas adsorption indicate that mesopore and micropore structures in shales are significantly altered due to thermal treatment at higher temperatures. In general, for both of the shales, initially, when treated at lower temperatures, with respect to the raw shales, the mesopore surface area and fractal dimensions were observed to increase with lowering of pore sizes and vice versa. Similar to the mesopore trend, the increase−decrease trend of microporosity with heating was observed to be consistent for both of the shales. The oil-window mature shales showed a significant increase in micropores compared to the thermally immature shales. Microstructural investigations using high-resolution imaging also indicated a dramatic alteration of visible porosity with thermal treatment.
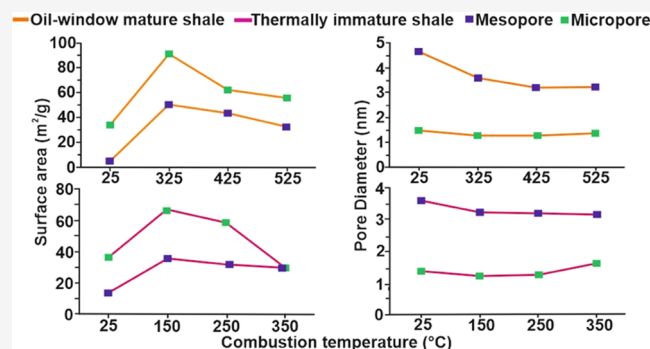
1. INTRODUCTION

Shale gas, due to its vast reserves and lower emission index compared to coal or oil, has become a crucial supplementary fuel for global energy supply.[1−4] Consequently, unconventional shale-petroleum systems continue to attract a lot of scientific interest.[5−18] Shale plays are characterized by heterogeneity and extremely low permeability (<nano-Darcy).[19−21] The highly heterogenous nature of shale plays result in a pore system that is complex and consists of a wide range of pore types and pore size distributions.[22−25] Shales mainly have three types of porosity: (i) pores present within the organic matter; (ii) interparticle: pores between mineral grains; and (iii) intraparticle: pores present within individual mineral grains.[6,26] These features of shale formation present difficulties in gas extraction because they have a direct impact on how gas behaves and is stored in the shale matrix.[27−29] Hydraulic fracturing (HF) is typically used to create a dense and extensive fracture network system (artificial permeability) that allows tight gas or oil to flow to the well bore.[30] However, improper monitoring and assessment of a shale gas reservoir for the pollutants produced during HF can have negative effects on the environment (e.g., contamination of under-

ground water), endangering the ecological balance.[30,31] For this reason, studies are being conducted to develop alternative solutions to HF for the safe extraction of shale gas from reservoirs.[32−34]

Several researchers have proposed combustion and pyrolysis techniques as alternatives to fracking because they can increase the permeability and porosity in shales.[26,29,32−35] Combustion or pyrolysis causes structural alteration of kerogen, resulting in the regeneration and reopening of pre-existing micro- and mesopores.[36,37] This leads to an increase in effective porosity, thereby improving gas flow in the matrix. Effect of pyrolysis on the pore attributes of shales has been the subject of many studies,[29,34,38−42] but evolution of shale characteristics after combustion has received limited attention.[26,29,33,34] In an experimental study conducted by Chen et al.[33] on mature shale

samples from the Yanshan region of China, it was observed that organic pores are removed during the oxidation of the organic material at temperatures of 400−500 °C. At even higher temperatures (≥600 °C), it has been reported that the diameter and volume of interparticle pores increase due to organic oxidization and decarbonation inside the shale.[43] After burning grounded shale samples for 5, 15, and 30 min at a fixed temperature of 500 °C, Chen et al.[26] found that the surface area decreased after combustion, while the average pore diameter increased with increasing oxidization time. Chandra et al.[34] in their study of Raniganj Basin shales found that oxic heating significantly increased the surface area and pore volume, whereas anoxic heating resulted in a significant decrease of both parameters due to pore blockage brought on by the presence of bitumen. In a separate study, Chandra et al.[29] emphasized that the increase in surface area and pore volume caused by oxic-heat treatment improves the long-term CO_2 storage viability in shales.

In this study, shales of contrasting thermal maturities from Raniganj and Bikaner−Nagaur basins are combusted for a fixed duration at different temperatures to investigate the evolution of porous structures, pore properties, and fractal dimensions. The heating temperatures are decided on the basis of the combustion behavior of the samples observed from thermogravimetric analysis (TGA). Low-pressure N_2 and CO_2 adsorption measurements at different experimental temperatures were analyzed to observe the changes in pore characteristics. Additionally, high-resolution imaging with a scanning electron microscope (SEM) was used to confirm these findings.

2. METHODOLOGY

2.1. Rock-Eval and Thermal Properties. A Rock-Eval 6 device was used to analyze the raw shales and the thermally treated splits (<212 μm size). The samples were analyzed using a modified version of the "basic/bulk-rock method" of Rock-Eval, with the ultimate oxidation temperature maintained at 750 °C.[44−46] The basic parameters such as free hydrocarbon (S1), heavier hydrocarbon (S2), thermal maturity level (T_{max}), and total organic carbon (TOC) were determined, while the hydrogen index [HI: (S2/TOC) × 100] was calculated.[47,48]

Thermogravimetric analysis were carried on with a NETZSCH STA 409C analyzer (NETZSCH, Germany) to produce thermograms from both differential scanning calorimetry (DSC) and thermogravimetry (TG-DTG) of the shales. In a crucible, 20 ± 0.1 mg of the samples was taken and heated under an atmosphere of air at the rate of 10 °C/min from room temperature to 750 °C. Several combustion characteristics, including ignition temperature (T_i, °C), burnout temperature (T_b, °C), and DSC and DTG peak temperatures (°C), were assessed from the TG-DTG and DSC thermograms. Temperatures with a mass loss rate of more than 1%/min at the start and end of the DTG thermogram were assumed ignition and burnout temperatures, respectively. Furthermore, kinetic parameters, such as preexponential factors (A), activation energy (E_a), and coefficients of determination (R^2), were calculated by fitting the weight loss curves with a first-order single-step reaction model with the help of NETZSCH Geratebau kinetic software.

2.2. Sample Types and Thermal Treatment. The two samples used in this study represent contrasting thermal maturities, sources, and organic compositions. Samples from the same study areas were previously studied by Singh et al.[49]

to examine the impact of degassing time and temperature on low-pressure gas adsorption-derived porosity interpretations. One sample (Rn-o-sh), collected from a borehole drilled at the Raniganj basin, Western India (coal basin with a dominant source of high-volatile bituminous coal), represents an oil-window mature shale (T_{max}: 441 °C) and marked by the presence of types II−III admixed kerogen (HI: 284 mg of HC/TOC). On the other hand, the other shale (Lig-o-sh), collected from the Barsingar lignite mines of the Bikaner−Nagaur basin in Eastern India, is thermally immature (T_{max}: 421 °C) and marked by the presence of type II kerogen (HI: 460 mg of HC/g TOC).

Based on their thermal properties and thermal maturity, the two shales were combusted at different temperatures. The Rn-o-sh shale was combusted for 30 min in a muffle furnace at 325, 425, and 525 °C to study the evolution of pore properties. The combusted products at 325, 425, and 525 °C are named Rn-325-sh, Rn-425-sh, and Rn-525-sh, respectively. The thermally immature Lig-o-sh shale was combusted for 30 min at 150, 250, and 350 °C to study the evolution of pore properties. The combusted products at 150, 250, and 350 °C are named as Lig-150-sh, Lig-250-sh, and Lig-350-sh, respectively.

2.3. Low-Pressure Gas Adsorption. Low-pressure gas adsorption (LPGA) study of the shale samples was carried out using the Quantachrome Autosorb iQ instrument. Properties of meso- and micropores of shales, such as pore volume, surface area, and size distribution, were measured using both N_2 and CO_2 as adsorbates. The two raw shales and their thermally treated counterparts were tested. The relative pressure of the adsorbate (P/P_0) rises gradually throughout the adsorption process until the adsorbate's condensation pressure is reached. Here, P_0 denotes the adsorbate's condensation pressure at a particular temperature and P represents the saturation pressure at each pressure point. The adsorbent's pore spaces become saturated with successive monolayers of adsorbate as the pressure is increased. A liquid N_2 bath with a temperature of 77 K and a saturation pressure of 1 bar was used for the N_2 LPGA experiment. In the P/P_0 range of 0.01−0.99, for each adsorption−desorption isotherm, a 40-point spread has been taken into account. The scope of learning about the micropores is constrained by the quadrupolar nature of N_2, which only has access to pores with a radius ≥1.3 nm. This is overcome by CO_2 LPGA by virtue of its ease of access and affinity toward micropores of shale. With a P/P_0 range of 0.0005−0.03, CO_2 LPGA takes place in a constant water bath at 273 K. Since CO_2 does not readily desorb from shale's micropores due to its higher affinity, adsorption isotherms with a 20-point spread have been calculated for each sample. The Brunauer, Emmett, and Teller (BET) specific surface area (SSA), Barrett−Joyner−Halenda (BJH) pore size distribution (PSD), and Frenkel−Halsey−Hill (FHH) fractal dimensions were determined by N_2 adsorption isotherms. Using the included software, the Dubinin−Astakhov (DA) pore volume, DFT PSD, the Dubinin−Radushkevich (DR) surface area, and other relevant parameters for micropore analysis were measured from the CO_2 isotherms.

2.4. Field Emission-Scanning Electron Microscopy and Image Analysis. Four cubic subspecimens of dimensions 2 mm × 2 mm × 2 mm were prepared from the Rn-o-sh and Lig-o-sh shales. Three of the four subspecimens of both Rn-o-sh and Lig-o-sh were heated at the desired temperatures, as mentioned in Section 2.1. After heating, once the samples were

Table 1. Results from Rock-Eval and Thermogravimetric Analyses of the Studied Shales

SN	S1 (mg HC/g rock)	S2 (mg HC/g rock)	T_{max} (°C)	TOC (wt %)	HI (mg HC/g TOC)	OI (mg CO_2/g TOC)	onset temperature (°C)	BOT (°C)	IT (°C)
Rn-o-sh	1.02	56.94	441	20.07	284	3	352.2	584.2	451.1
Rn-325-sh	0.14	0.55	563	13.72	4	10			
Rn-425-sh	0.27	0.16	609	8.48	2	5			
Rn-525-sh	0.28	0.06	282	5.63	1	3			
Lig-o-sh	1.68	87.01	421	18.91	460	52	191.4	398.6	284.7
Lig-150-sh	0.28	8.91	431	13.37	67	43			
Lig-250-sh	0.07	0.51	469	4.19	12	47			
Lig-350-sh	0.02	0.21	447	1.51	8	39			

cooled down to room temperature, they were mechanically polished to produce smooth surfaces. These were then gold-coated (duration: 2 min) and inserted into the Carl Zeiss Merlin VP Compact field emission-scanning electron microscope (FE-SEM). The samples were examined under both secondary electron (SE2) and AsB (angle selective back-scattered) modes to understand the evolution of structures within the thermally treated shales in comparison to the raw samples. During imaging, the working distance and resolution were kept constant. The steps followed to extract the information on pore diameter using the image analysis technique are as follows.

(1) Initially, secondary electron images (SE2) were imported and converted to binary images using ImageJ-Fiji software.

(2) Afterward, pores in the SE2 images were segmented using the Trainable Weka Segmentation (TWS) plugin in ImageJ. TWS works based on classifier based machine learning algorithms. Here, we assigned two different classifiers to train and distinctly segment pores from the matrix in individual images.

(3) After segmentation, area fraction, i.e., the ratio between the total area of the pores with respect to the total area of the image, was determined to estimate the porosity (%) of the individual sample.

(4) Finally, different properties of the individual pores (such as area, maximum and minimum diameters) corresponding to each SE2 image were extracted to identify maximum and minimum sizes of the pores.

3. RESULTS AND DISCUSSIONS

3.1. Nature of Samples. Table 1 presents the results from the Rock-Eval analysis and basic thermal properties of the two shales used in this study. As previously mentioned, the two samples used in this study represent contrasting thermal maturities, sources, and organic compositions. For the oil-window mature shale from the Raniganj basin (Rn-o-sh), the onset temperature of oxidative thermal decomposition, ignition temperature, and burnout temperature were observed to be 352.2, 451.1, and 584.2 °C, respectively. Consequently, temperatures of 325, 425, and 525 °C were selected for combustion of this shale to study the evolution of pore properties. For the thermally immature shale from the Bikaner−Nagaur basin (Lig-o-sh), the onset temperature of oxidative thermal decomposition, ignition temperature (IT), and burnout temperature (BOT) were observed to be 191.4, 284.7, and 398.6 °C, respectively. Consequently, temperatures of 150, 250, and 350 °C were selected for combustion of this shale to study the evolution of pore properties.

The samples used in the study clearly present the importance of thermal maturity level on in situ combustion of shale horizons. For the oil-window shale (Rn-o-sh), it can be observed that with increasing temperatures of thermal treatment (325, 425, and 525 °C), the TOC decreases systematically (Table 1). On the other hand, for the thermally immature shale (Lig-o-sh), even though treated at lower temperatures (150, 250, and 350 °C), the decrease in TOC is even sharper with increasing temperatures of treatment (Table 1). While this further establishes the rationale of using different treatment temperatures for the shales used in this study, it also indicates that different heating programs should be adopted for in-combustion of shales, depending on their thermal maturity levels and organic matter type.

Different kerogen types have different structures, and consequently, their responses to heating would be different. Types I−II kerogen, marked by higher initial hydrogen contents, comprise long-chained aliphatics and consequently react at lower temperatures generating oil and gas.[50,51] In contrast, types III−IV kerogen are marked by lower hydrogen and higher carbon contents, comprise polycyclic aromatic structures, and require higher temperatures to react for generating hydrocarbons.[51,52] The different chemistry and structure of kerogen types will essentially control their differential behaviors at changing temperatures. While a lower temperature may be sufficient for stimulating a type I−II kerogen bearing shale horizon, a much higher temperature would be needed for stimulating a type III−IV kerogen bearing shale horizon. Similarly, the impact of thermal maturity of organic matter can also be significant. For the sets of shales used in this study, the oil-window mature shale, owing to its higher thermal maturity level, requires higher temperatures to react/convert. Increasing thermal maturity is accompanied by an increase in carbon content and aromaticity, a decrease in hydrogen and oxygen contents, and a reduction in the aliphaticity of organic matter. For samples with even higher thermal maturities, even higher temperatures would be needed for the shales to react and facilitate in situ conversion. Previous studies by İnan et al.[53] and Hazra et al.[54] have demonstrated that higher temperatures are required for thermally mature and overmature shales to react under oxidizing conditions. Using Rock-Eval and thermal analyses, Hazra et al.[54] demonstrated that with increasing thermal maturity of shales, the temperature peak of decomposition under oxidizing conditions increases. Consequently, while targeting the in situ conversion of shales, heating plans should be adopted considering the kerogen chemistry and thermal maturity.

3.2. Inferences from Low-Pressure Nitrogen Gas Adsorption. *3.2.1. Impact of Thermal Treatment on Oil-Window Mature Shale (Rn-o-sh) and Its Thermally Treated*

Table 2. Pore Structural Parameters Derived Using Low-Pressure Nitrogen Gas Adsorption

| sample number	BET SSA (m^2/g)	BJH pore volume (cc/g)	BJH pore diameter (nm)	average pore radius (nm)	fractal dimension (D1)	fractal dimension (D2)
Rn-o-sh	4.19	0.009	4.648	9.474	2.54	2.64
Rn-325-sh	49.908	0.016	3.588	3.162	2.81	2.92
Rn-425-sh	43.056	0.025	3.209	4.190	2.82	2.84
Rn-525-sh	32.601	0.03	3.218	5.383	2.74	2.79
Lig-o-sh	13.793	0.073	3.616	21.667	2.33	2.44
Lig-150-sh	35.743	0.083	3.244	10.649	2.69	2.61
Lig-250-sh	31.658	0.085	3.209	12.112	2.67	2.58
Lig-350-sh	29.821	0.064	3.165	9.65	2.52	2.65
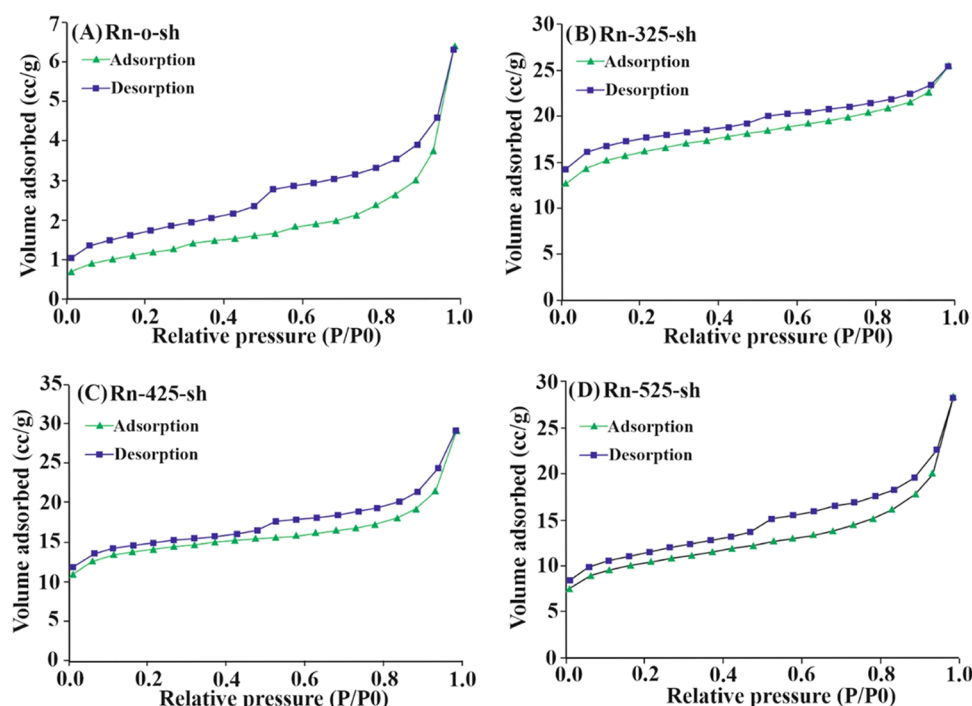
Figure 1. Low-pressure nitrogen gas adsorption and desorption isotherms of the oil-window mature shale and the thermally treated counterparts.

Counterparts. For the untreated Rn-o-sh shale from the Raniganj basin, the BET SSA was observed to be 4.19 m^2/g rock (Table 2). The nature of the adsorption isotherm was observed to be Type IIb (Figure 1A).[55] For the same sample, when heated to 325 °C (Rn-325-sh), a marked change in the adsorption isotherm was noted (Figure 1B). A manifold increase in the adsorption capacity was noted at the lowest experimental pressures, thereby substantiating a marked increase in microporosity of the sample owing to thermal treatment. For the split treated at 325 °C, the BET SSA was observed to increase to 49.91 m^2/g rock. This change is BET SSA, and the adsorption isotherm is also manifested in the BJH pore size distribution (PSD) plot, where it can be observed that for the Rn-325-sh sample, the volume of pores in the smaller sizes (~10 nm) is several times larger compared to the Rn-O-sh sample (Figure 2A). Moreover, the BJH pore volume and the average pore diameter were observed to strongly increase and decrease, respectively, for the Rn-325-sh shale (0.016 cc/g and 3.16 nm) compared to the Rn-O-sh shale (0.009 cc/g and 9.47 nm). What this essentially indicates is that owing to oxidation at 325 °C, due to the conversion/reaction of organic matter, a large number of smaller mesopores are created, which thereby impart a larger SSA for the Rn-325-sh sample compared to the Rn-O-sh shale.

Compared to the Rn-325-sh split, the sample heated to 425 °C (Rn-425-sh) showed a decrease in BET SSA and an increase in pore size, although the pore volume determined by the BJH model was observed to be higher. The nature of the adsorption isotherm was observed to be markedly different for the Rn-425-sh split (Figure 1C), with a steeper slope noted at higher relative pressures, indicating formation of coarser pore spaces. Closer examination of the PSD plot determined using the BJH model revealed that in contrast to the Rn-325-sh split (Figure 2), where a decreasing trend was observed from smaller pores to larger pores, for the Rn-425-sh split (Figure 2), an increasing trend was observed from the smaller mesopores to the larger mesopores. What this indicates is that owing to thermal treatment at 425 °C, alteration of organic matter takes place, resulting in formation of larger mesopores.

When the same sample was heated to 525 °C (Rn-525-sh), significant changes were observed in the adsorption isotherm (Figure 1D), PSD, and other pore properties, compared to the other splits. The volume of gas adsorbed at the lowest experimental pressure dropped by approximately 40% and 30%, compared to the Rn-325-sh and Rn-425-sh splits, respectively. This indicates that a significant reduction in microporosity takes places owing to heating the samples at 525
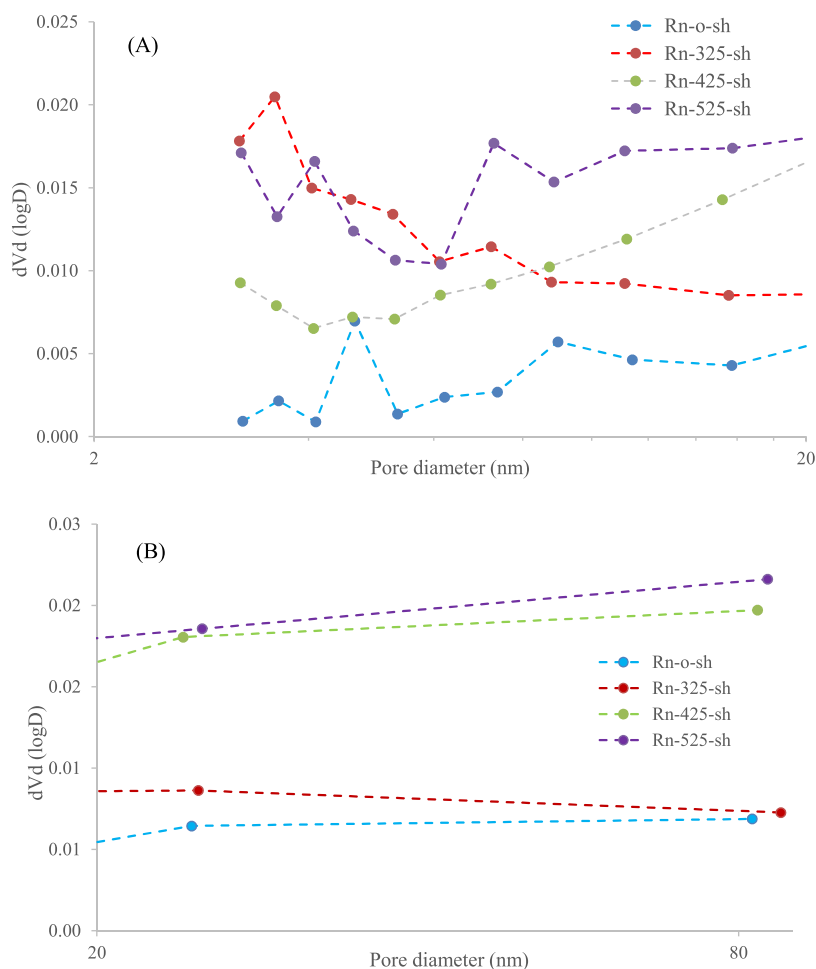
Figure 2. Pore size distribution (PSD) plots [$dV\,d(\log d)$ vs pore diameter] of the Rn-o-sh shale and the thermally treated counterparts derived using the BJH adsorption model; (A) shows the PSD for pore diameter varying between 2 and 20 nm, and (B) shows the PSD for pore diameter ≥20 nm.

°C. Consequently, the BET SSA for Rn-525-sh dropped to 32.60 m²/g, while the average pore radius increased to 5.38 nm. This can be attributed to heating the sample at higher temperatures, resulting in combustion of the organic matter causing alteration of their pore spaces, and formation of larger pores. Interestingly, for Rn-525-sh, the BJH pore volume was observed to increase compared to the other splits. The PSD from the BJH model for this split substantiates increased pore openings, especially at sizes exceeding 5 nm, owing to thermal treatment at 525 °C (Figure 2).

3.2.2. Impact of Thermal Treatment on Thermally Immature Shale (Lig-o-sh) and the Thermally Treated Counterparts. For the untreated thermally immature shale collected from the lignite mine (Lig-o-sh), the BET SSA was observed to be much higher compared to the Rn-o-sh shale. For the untreated split, while the BET SSA was observed to be 13.79 m²/g, for the split treated at 150 °C (Lig-150-sh), the same was observed to increase to 35.74 m²/g (Table 2). While the nature of the adsorption isotherm was similar for both splits (Figure 3), a closer examination of them reveals that the adsorption capacity significantly increased (∼5 times) for Lig-150-sh at the lowest experimental pressures. This indicates formation of finer mesopores, and/or micropores, due to thermal treatment of the thermally immature shale at 150 °C. While the nature of pore size distribution obtained from the BJH model was similar for both splits, a larger volume of finer

mesopores was observed within Lig-150-sh, relative to the Lig-o-sh split (Figure 4). Consequently, the average pore diameter was observed to drop to 10.65 nm for Lig-150-sh, compared to 21.67 nm for the untreated split.

A drop in volume of the gas adsorbed at the lowest experimental pressures was noted for the Lig-250-sh split, compared to the Lig-150-sh split, indicating closure of some pore spaces due to thermal treatment at 250 °C. Consequently, the BET SSA was observed to decrease from 35.43 m²/g (for Lig-150-sh) to 31.66 m²/g (for Lig-250-sh), along with an increase in the average pore diameter to 12.11 nm. When the temperature of treatment was increased to 350 °C (Lig-350-sh), a decrease in adsorption capacity at the lowest experimental pressures was noted, indicating closure of some finer mesopores owing to thermal treatment at higher temperatures. Consequently, the BET SSA of the sample was observed to decrease. Interestingly, the highest volume of gas adsorbed was also observed to decrease significantly (46.52 cc/g) compared to Lig-250-sh (61.97 cc/g) and Lig-150-sh (61.52 cc/g). Further, the average pore diameter was observed to decrease for Lig-350-sh compared to the other splits. What these indicate is possible closure/collapse of pore structures owing to heat treatment at an elevated temperature of 350 °C. This inference is also supported by the strong drop in the BJH pore volume detected for Lig-350-sh (0.064 cc/g). This behavior is likely considering the thermal characteristic of the
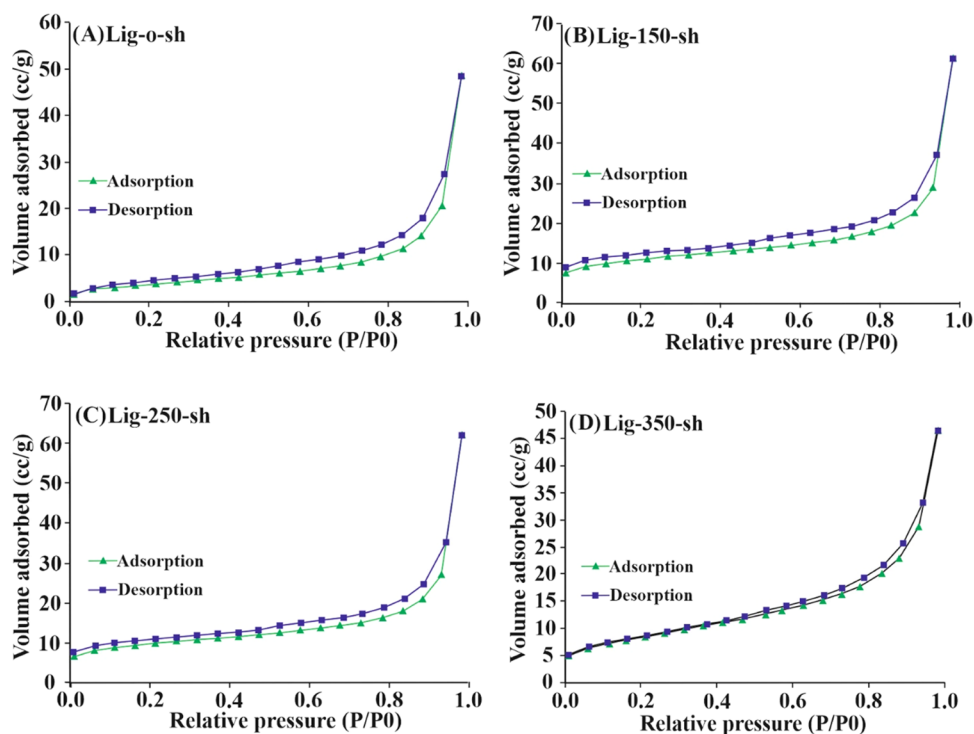
Figure 3. Low-pressure nitrogen gas adsorption and desorption isotherms of the thermally immature shale and the thermally treated counterparts.

shale. As mentioned previously, the thermally immature shale (Lig-o-sh) is marked by ignition and burnout temperatures of 284.7 and 398.6 °C, respectively. When heated to a temperature of 350 °C, a major fraction of the organic matter within the shale is burnt off, and consequently, the pore spaces created within the sample at previous examination temperatures of 150 and 250 °C would be altered/lost due to collapse of the structure. The loss in organic matter for Lig-350-sh is also indicated by the low TOC yield of the sample (2.51 wt %; Table 1). Further, this sample also showed a low difference in contrast among the different constituents when examined under FE-SEM using the angle selective backscattered (AsB) mode (see Section 3.4). Ideally, when examined under FE-SEM using AsB, organic matter and mineral matter show contrasting gray levels, with organic matter showing a darker interference and inorganic matter showing a brighter interference owing to their differences in atomic numbers.[18]

A closer examination of PSD obtained from the BJH model for the Lig-o-sh shale and its thermally treated splits provides deeper insights into the above inferences. Figure 4 shows the $dV/d\log(d)$ vs pore diameter plot (PSD plot), obtained using the BJH model, of the thermally immature shale and its thermally treated splits. For ease of understanding, the plot has been divided into two parts: (a) PSD in the 2−20 nm size range (Figure 4A), and (b) PSD in the 20−80 nm size range (Figure 4B). In Figure 4A, it can be seen that the volume of pores is minimal for the untreated raw shale (Lig-o-sh). As discussed earlier, the volume increases for the Lig-150-sh split and then drops for the Lig-250-sh split. However, the volume again sharply increases in the 2−20 nm range for the Lig-350-sh split. In contrast, a distinctive trend was observed for the PSD in the 20−80 nm size range (Figure 4B). In this range, the highest volume of pores is shown by the Lig-250-sh split, followed by the Lig-150-sh split. It is due to this reason the volume of pores was observed to be higher for the Lig-250-sh

split. For the Lig-350-sh split, a massive drop in the volume of pores is observed in the 20−80 nm size range, even lower than the untreated Lig-o-sh sample. This sudden drop is caused due to collapse of the structure, owing to the near-complete burnout of the organic matter present within the sample.

3.2.3. Changes in Fractal Dimensions due to Thermal Treatment. For both samples, considerable changes in fractal dimensions were observed with changing thermal treatment temperatures. For the oil-window mature untreated sample (Rn-O-sh), D1 (2.54; lower relative pressure, surface fractal dimension) and D2 (2.64; higher relative pressure, pore structural fractal dimension) were observed to be small (Table 2). However, when thermally treated, D1 was observed to strongly increase for the Rn-325-sh split (2.81) and then gently increase for the Rn-425-sh split (2.82), followed by a sharp decrease for the Rn-525-sh split (2.74). D2, on the other hand, was observed to systematically increase for the Rn-325-sh (2.92) split, followed by a sharp decrease for Rn-425-sh (2.84) and Rn-525-sh (2.79) splits (Table 2). Figure 5 plots the fractal dimensions of the shales obtained from the FHH model. The changing nature of D1 and D2 is in line with the changes in BET SSA (first increase for the Rn-325-sh split and then decrease with higher temperatures of treatment; Figure 5) and the average pore diameter (first decrease for the Rn-325-sh split and then increase with a higher temperature of treatment; Figure 6).

For the untreated thermally immature shale (Lig-o-sh), initially, the fractal dimensions D1 (2.33) and D2 (2.44) were observed to be small. However, when thermally treated at 150 °C (Lig-150-sh), D1 and D2 were observed to strongly increase to 2.69 and 2.61, respectively, indicating formation of complex pore structures caused by thermal treatment. When the temperature of treatment was increased to 250 °C, both D1 and D2 were observed to decrease to 2.67 and 2.58, respectively. This change (drop) is consistent with the drop in
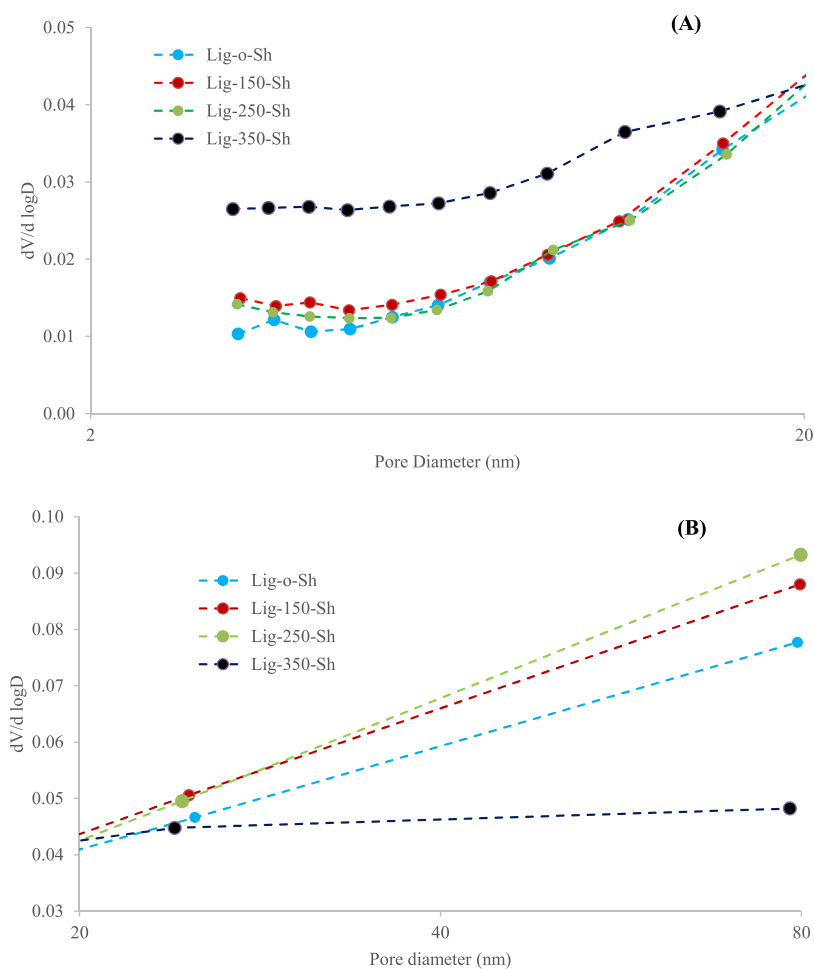
Figure 4. Pore size distribution (PSD) plots [dV d(log d) vs pore diameter] of the Lig-o-sh shale and the thermally treated counterparts derived using the BJH adsorption model; (A) shows the PSD for pore diameter varying between 2 and 20 nm, and (B) shows the PSD for pore diameter ≥20 nm.
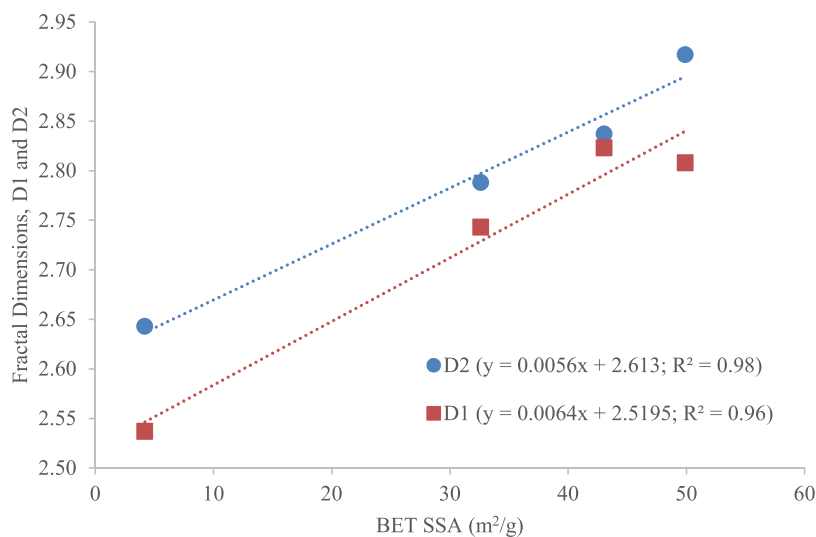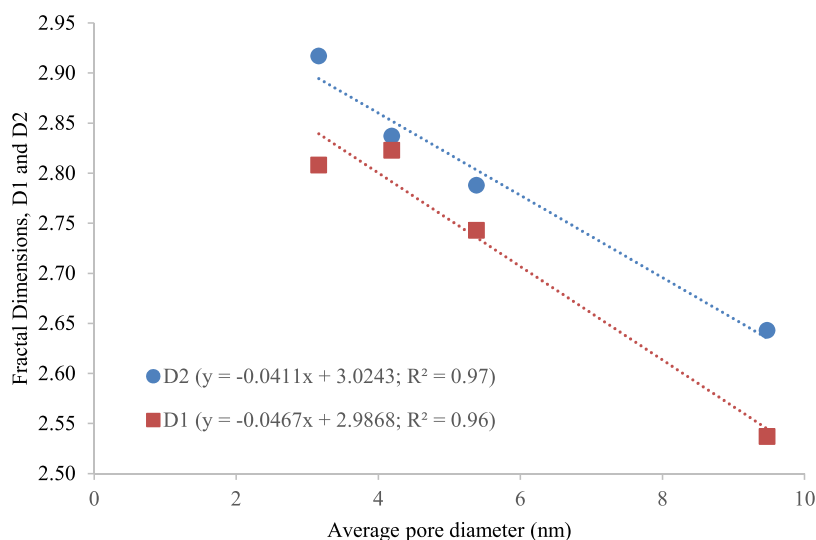

Figure 5. Cross-plot showing the relationship between BET SSA and fractal dimensions D1 and D2 for the oil-window mature shale and its thermally treated splits.

BET SSA and pore diameter for the Lig-250-sh split, relative to the Lig-150-sh split. However, for the Lig-350-sh split, while the D1 was observed to further drop sharply (2.52), D2 was observed to increase (2.65). This is in contrast to the

decreasing D2 with increasing temperature of treatment of the other samples. This increment in D2 could be attributed to the collapse of the structure of the shale owing to treatment at 350 °C, resulting in a decrease of the BET SSA and BJH pore

Figure 6. Cross-plot showing the relationship between the average pore diameter and fractal dimensions D1 and D2 for the oil-window mature shale and its thermally treated splits.

Figure 7. Cross-plot showing the relationship between BET SSA and fractal dimensions D1 and D2 for the immature shale and its thermally treated splits. Note: The increasing sizes of the sample symbols indicate increasing temperatures of thermal treatment.
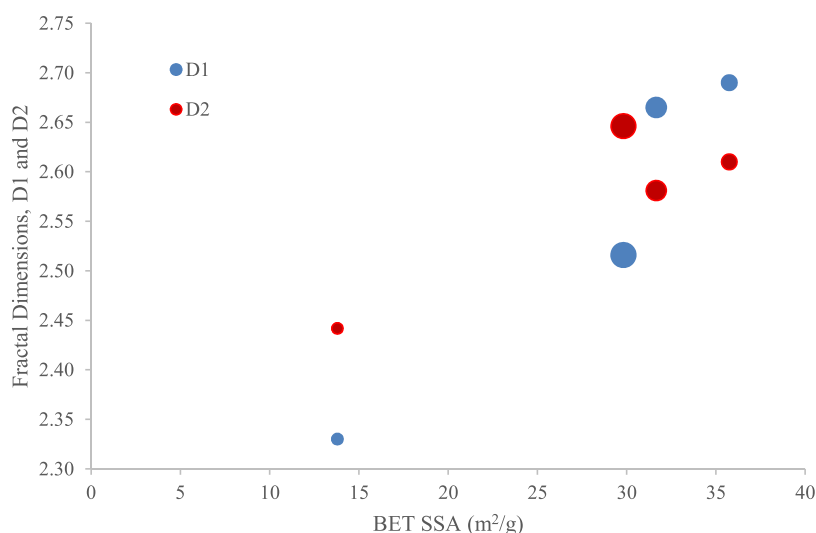
volume (as discussed previously) and an increase in D2. Figures 7 and 8 plot the changing nature of D1 and D2 with BET SSA and the average pore diameter for the Lig-o-sh and the thermally treated splits.

3.3. Inferences from Low-Pressure Carbon Dioxide Gas Adsorption. Low-pressure CO_2 adsorption experiments of the untreated and thermally treated shales were carried out to examine the changes in micropore properties with temperature. The isotherms in general can be classified as type II with a higher adsorption rate at a lower relative pressure. The 150 °C-heated thermally immature shale (Lig-150-sh) shows a significant increase (more than 2×) in CO_2 uptake compared to its untreated counterpart (Lig-o-sh). However, the adsorption capacity decreases uniformly with increasing temperature up to 350 °C (Figure 9). The CO_2 uptake of the untreated Rn-o-sh shale is lower than that of the immature Lig-o-sh shale; however, at 325 °C, the adsorption potential increases more than 300%, indicating significant formation of micropores (Figure 9). With a further increase in

temperature, the adsorption potential steadily decreases at 425 and 525 °C (Table 3).
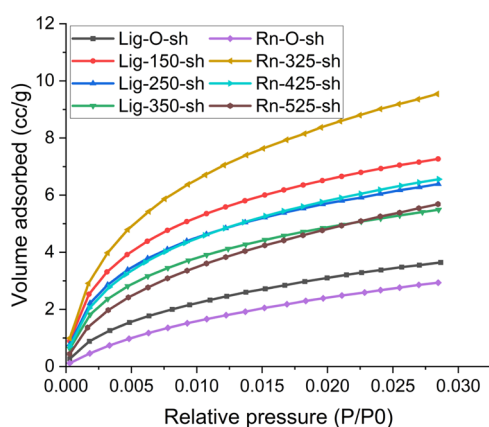
Although the increase−decrease trend with heating is consistent for both shales, it is evident that the oil-window mature Rn shales show a significant increase in micropores compared to the thermally immature shales. An identical increase was observed for the mesopores with N2-LPGA in the earlier section.

As expected, the DR surface area and the DA pore volume follow a similar increase−decrease trend for both immature and mature shales (Figure 10). The surface area for immature shales increases from 33.6 to 66.8 m²/g, which is similar to the 2× increase in the adsorption potential for these shales. The magnitude of increase in pore volume however does not match the magnitude of increase in surface area, which indicates a significant increase in micropore surface roughness for both existing pores and newly created pores. This observation is similar to the mesopore surface fractal dimension calculated using the FHH model. With a further increase in temperature beyond 150 °C, the surface area decreases by ∼8 m²/g with
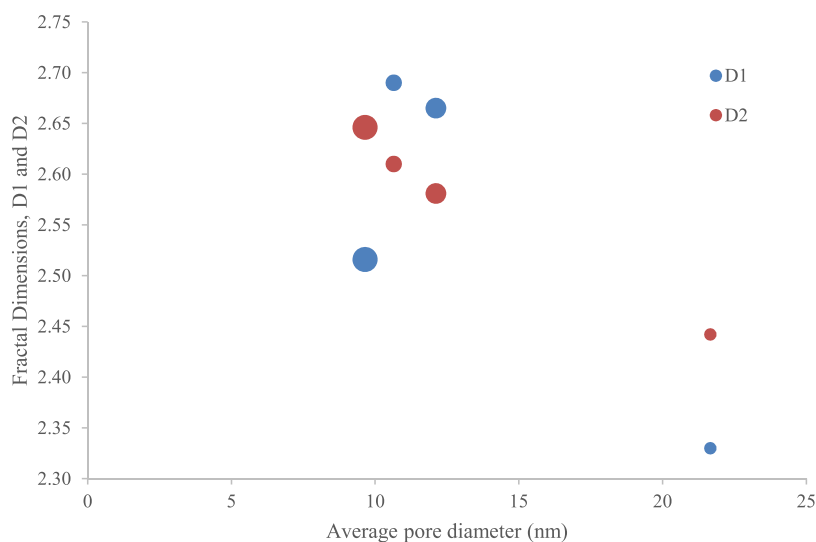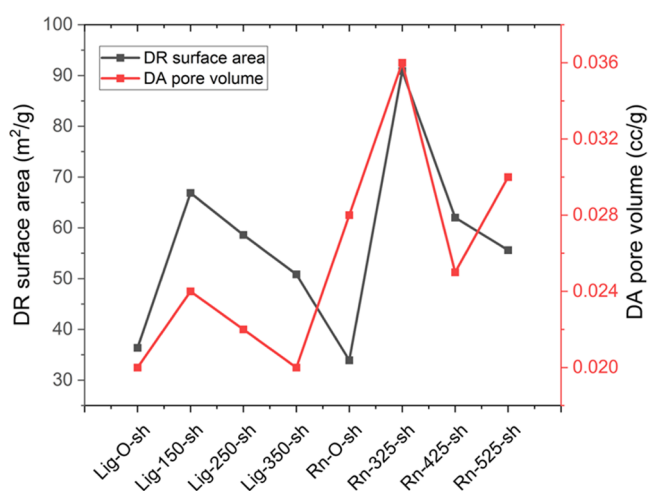
Figure 8. Cross-plot showing the relationship between average pore diameter and fractal dimensions D1 and D2 for the immature shale and its thermally treated splits. Note: The increasing sizes of the sample symbols indicate increasing temperatures of thermal treatment.

Figure 9. Low-pressure CO_2 gas adsorption isotherms of the shales used in this study.

Figure 10. Plot showing the variation in the DR surface area and DA pore volume for the studied shales.

each 100 °C increase (Figure 10). A similar behavior is observed for the mature Rn shales, where a comparison of pore volume and surface area change indicates enhancement of micropore surface roughness. Interestingly, although the surface area increase−decrease trend is similar to the isotherms, the change in pore volume requires further attention. The pore volume of Rn-425-sh is evidently lower than that of the untreated Rn shale; however, the surface area is higher than that of the Rn-o shale. This indicates that pores having a higher volume/surface area, i.e., pores with smoother

surfaces, are converted to mesopores, and pores with rougher surfaces contribute primarily in the micropore range. Reversal of the trend with a further 100 °C increase in temperature (Rn-525-sh) indicates that the surface of the pores is gradually smoothened with increasing temperature.

The pore size distributions for the micropores were calculated using the CO_2-based DFT model. The peaks in pore sizes are roughly uniform for all samples. For the

Table 3. Pore Structural Parameters Derived Using Low-Pressure CO_2 Gas Adsorption

sample number	D−R micropore surface area (m²/g)	D−R micropore volume (cc/g)	D−R pore width (nm)	D−A micropore volume (cc/g)	D−A pore diameter (nm)	DFT surface area (m²/g)	DFT pore volume (cc/g)	DFT pore width (nm)
Rn-o-sh	33.925	0.013	0.937	0.028	1.50	29.715	0.009	0.479
Rn-325-sh	90.898	0.034	0.776	0.036	1.26	100.481	0.028	0.349
Rn-425-sh	62.017	0.023	0.773	0.025	1.26	68.728	0.019	0.349
Rn-525-sh	55.603	0.021	0.824	0.03	1.36	60.993	0.019	0.349
Lig-o-sh	36.378	0.014	0.835	0.02	1.36	38.021	0.011	0.349
Lig-150-sh	66.873	0.025	0.742	0.024	1.22	75.555	0.02	0.349
Lig-250-sh	58.617	0.022	0.747	0.022	1.24	66.854	0.018	0.349
Lig-350-sh	29.838	0.011	0.907	0.039	1.62	30.09	0.01	0.573

immature Lig shales, the increase in pore volume is evident in the 0.3 and 0.4−0.6 nm ranges; however, the increase in pore volume is negligible in the larger pore size range (0.7−1.6 nm), which indicates formation of predominantly smaller micropores with increasing temperatures (Figure 11). An increase in
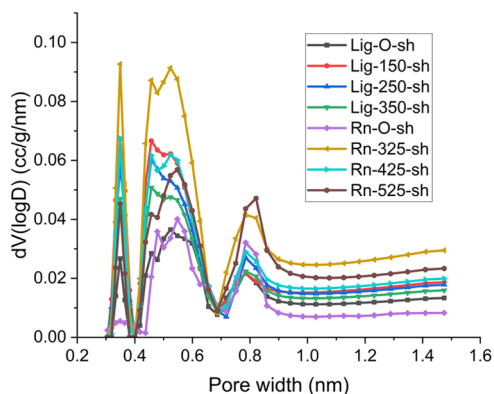
Figure 11. Pore size distribution plots $[dV(\log d)$ vs pore width$]$ of the studied shales derived using the DFT model.

temperature from 150 to 250 °C shows a decrease in the pore volume in the 0.4−0.6 nm range; however, an increase in pore volume is observed beyond 0.7 nm, which indicates that the formation of new pores is slowed down and an enlargement of existing pores begins. Further increase in temperature (Rn-350-sh) shows a uniform reduction of pores beyond 0.4 nm pore width, which indicates that most micropores are being converted into mesopores. For the mature Rn shales, the untreated sample shows a very low smaller micropore volume, which increases significantly at 325 °C (Figure 11). A further 100 °C increase in temperature decreases the overall micropore volume because of enlargement of existing micropores to mesopores and lack of formation of new pores. With a further increase in temperature (Rn-525-sh), the smaller

micropores decrease and pores larger than 0.7 nm width increase.

3.4. Microstructural Observations Using FE-SEM.

3.4.1. Microstructural Changes due to Thermal Treatment on Oil-Window Mature Shale (Rn-o-sh).

For the untreated Rn-o-sh shale, unaltered organic matter with very few small microcracks was found dispersed throughout the sample (Figure 12A). The dimension of the microcracks was in the range of 2−100 μm in length and 0.3−1.5 μm in width (Table 4). When the same sample was heated at 325 °C (Rn-325-sh),

Table 4. Summary of the Pore Property Variations Observed through FE-SEM

sample number	dominantly observed pore shape		average pore diameter	
	micropores	macropores	micropores (μm)	macropores (μm)
Rn-o-sh		microcracks		length: 2−100
				width: 0.3−1.5
Rn-325-sh		microcracks		length: 14−426
				width: 0.2−2.3
Rn-425-sh	spherical	spherical	0.006−0.01	1−3.87
	elongated	elongated	0.002−0.04	1−2.68
Rn-525-sh	spherical	spherical	0.001−0.03	1−7.2
	elongated	elongated	0.001−0.06	1−3.6
Lig-o-sh				
Lig-150-sh	spherical	indents	0.3−0.7	0.2−2.8
	elongated		0.2−0.4	
Lig-250-sh	spherical	spherical	0.002−0.06	1.5−7.4
	elliptical	elongated	0.004−0.03	1.6−4.47
Lig-350-sh	spherical	spherical	0.002−0.04	1.2−2.3
	elongated	elongated	0.005−0.07	1.1−1.9

an altered microstructure was observed (Figure 12B). Organic matter in this sample exhibited a rapid increase in the number of microfractures; as a result, a sharp increase in visible porosity was detected from 3.6 to 14.7% under 1500×
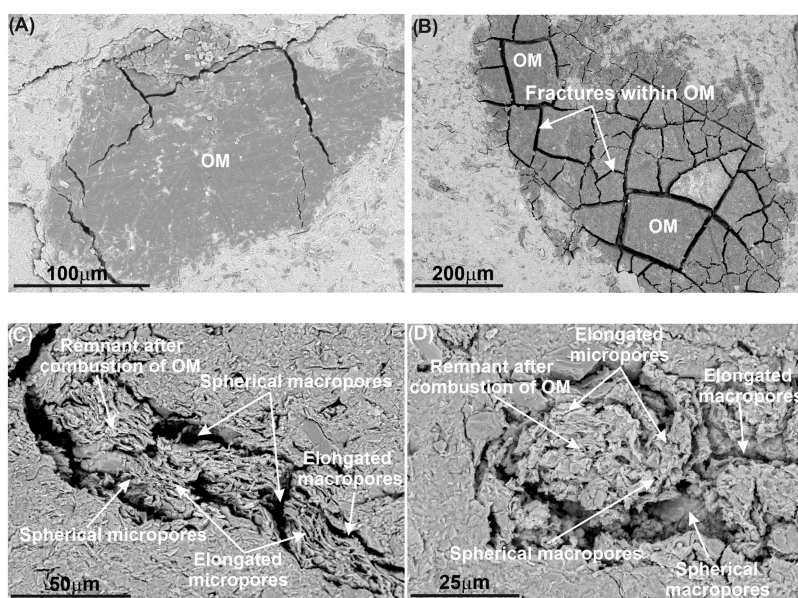
Figure 12. Microstructural evolution of mature shale due to heat treatment. (A−D) represent microstructures of Rn-O-sh, Rn-325-sh, Rn-425-sh, and Rn-525-sh, respectively. Here, OM denotes organic matter.
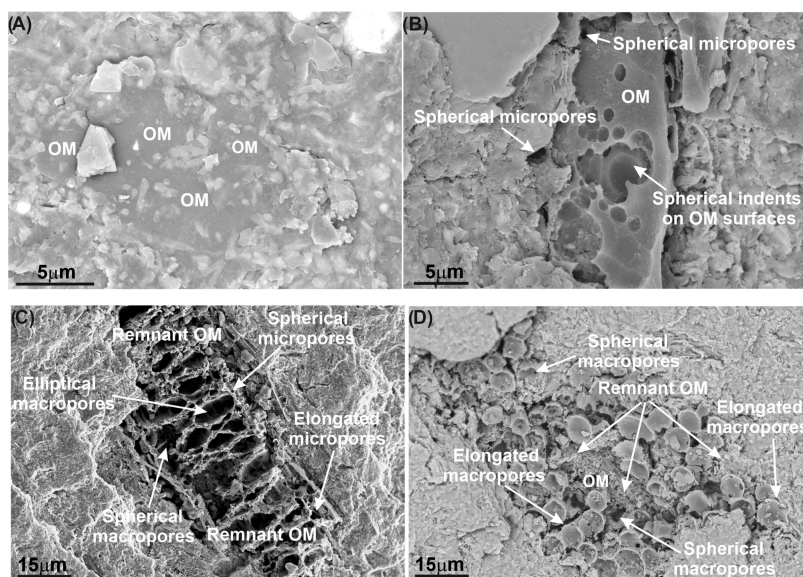
Figure 13. Microstructural evolution of immature shale due to heat treatment. (A−D) represent microstructures of Lig-O-sh, Lig-150-sh, Lig-250-sh, and Lig-350-sh, respectively. Here, OM denotes organic matter.

magnification (based on image analysis using ImageJ software) due to heat treatment. The dimension of the microcracks in this sample was 14−426 μm in length and 0.2−2.3 μm in width under 1500× magnification (Table 4). It is apparent that the increase in the number of microcracks under FE-SEM is caused due to the release of volatiles from the organic matter during heat treatment.

Due to thermal treatment of the sample at 425 °C (Rn-425-sh), a dramatic microstructural alteration was observed (Figure 12C). Organic matter appeared to be burnt out, to a large extent, leaving the remnant of it, as the contrast between the mineral matter (brighter interference under AsB) and organic matter (darker interference under AsB) was largely reduced. As a result, four new types of pores developed: (1) spherical-shaped larger macropores, (2) elongated larger macropores, (3) small elongated micropores, and (4) small spherical micropores within the remnant organic matter and clay particle interfaces. Using the image analysis technique, the average diameters of these four types of pores were estimated to be 1−3.87, 1−2.68, 0.002−0.04, and 0.006−0.01 μm, respectively, under 1500× magnification. It was estimated that the combustion of the organic matter at 425 °C (Rn-425-sh) caused an increase in the overall visible porosity up to 21.28% with respect to the untreated Rn-O-sh shale under 1500× magnification.

Rn-525-sh exhibited a significant reduction in the total volume of organic matter due to burnout of the organic matter (Figure 12D). This is also supported by its very low TOC content (5.63 wt %; Table 1). Similar to Rn-425-sh, this sample also displayed evidence of four types of pores: (1) spherical-shaped larger macropores, (2) elongated larger macropores, (3) small elongated micropores, and (4) small spherical micropores. Using the image analysis technique, it was observed that the diameter of the macropores ranges up to 7.2 μm, which is larger compared to the sample heated at 425 °C. Interestingly, the sample displayed a significant reduction in the number of small elongated and spherical micropores caused due to structural collapse owing to heat treatment. The observations from FE-SEM corroborate the findings from low-pressure nitrogen gas adsorption.

3.4.2. Microstructural Changes due to Thermal Treatment on Thermally Immature Shale (Lig-o-sh). Microstructural investigations suggest that the oil-window mature shale (Rn-o-sh) and immature shale (Lig-o-sh) followed slightly different paths of alteration due to heat treatment. Initially, at room temperature, the immature shale (Lig-O-sh) exhibited intercalation of unaltered organic matter, silicate particles, and clay on the sample surface (Figure 13A). With increasing temperature due to heat treatment at around 150 °C (Lig-150-sh), spherical and elongated small micropores developed within the organic matter as well as at the interface of organic matter and silicate minerals (Figure 13B). The diameter of these small micropores varied in the range between 0.05 and 0.7 μm under 1500× magnification (Table 4). Apart from these small micropores, spherical indents on the altered organic matter surface were also prominent (Figure 13B), the diameter of which varied in a wide range from 0.2 to 2.8 μm under 1500× magnification (Table 4). It appeared that larger indents developed due to aggregation of multiple small spherical indents. Release of the structural volatile from the organic matter during heat treatment possibly triggered development of such aggregated indent microstructures.

Due to heat treatment at 250 °C (Lig-250-sh), a significant increase in the overall visible porosity up to 23.8% under 1500× magnification was observed (Figure 13C). The remnant organic matter (OM) within the sample exhibited a fused microstructure. Four different types of pore morphologies were identified within the remnant organic matter after combustion: (1) elliptical larger macropores, (2) spherical larger macropores, (3) spherical small micropores, and (4) elongated small micropores. Sizes of these four different pore types varied in the ranges of 1.6−4.47, 1.5−7.4, 0.002−0.06, and 0.004−0.03 μm, respectively, under 1500× magnification.

Lig-350-sh displayed relatively less organic matter under FE-SEM compared to the earlier samples as combustion of the sample at 350 °C resulted in loss of organic carbon (also indicated by its low TOC content of 1.51 wt % (Table 1)). Interestingly, on increasing the temperature up to 350 °C (Lig-350-sh), a sharp decrease in visible porosity was observed (Figure 13D). This sample exhibited visible porosity of only

13.29% at 1500× magnification, which was less compared to that of Lig-250-sh. Four different types of pore morphologies were identified: (1) spherical larger macropores, (2) elongated larger macropores, (3) spherical smaller micropores, and (4) elongated smaller micropores. Their size ranges were 1.2−2.3, 1.1−1.9, 0.002−0.04, and 0.005−0.07 μm, respectively, under 1500× magnification. It was evident from the microstructural observation that the size as well as the number of macropores is less in this sample compared to Lig-250-sh, which probably caused a rapid reduction in the total visible porosity. Reduction in visible porosity in this sample could be due to structural collapse owing to heat treatment at 350 °C.

4. CONCLUSIONS

- While the two shales of different thermal maturities used in this study show complex evolution with changing temperatures of thermal treatment, the temperature protocols in the experiments establish that the heating programs for in situ conversion of shales should base themselves on the thermal maturity stage of the shales.

- With increasing temperatures of treatment, the mesopore surface area increases initially (by approximately 1200% for oil-window mature shale and 160% for thermally immature shale) and then decreases (by approximately 35% for oil-window mature shale and 16% for thermally immature shale), indicating formation of smaller pores and their continued enlargement. The only exception was the Lig-350-sh sample, which possibly burnt much of the organic matter, and the concomitant alteration and collapse of the organic matrix pores.

- The increase−decrease trend of microporosity with heating was observed to be consistent for both shale types. The oil-window mature shale shows a significant increase in micropores (approximately 168%) compared to the thermally immature shale (approximately 83.82%).

- Microstructural analysis of shale samples under SEM revealed decreasing discernability between organic and mineral matter with increasing temperature. The pore morphology of the oil-window mature shale with increasing treatment temperatures evolves from large, elongated microcracks to complex pore networks comprising micro- and macropores, before finally collapsing at the highest treatment temperature. In contrast, the pore morphology of the thermally immature shale follows a slightly different path during heat treatment and exhibits discrete small micropores (0.3−0.7 mm) to dense micropores (0.002−0.03 mm) and macropore networks (1.1−2.3 mm) prior to the eventual collapse.

■ AUTHOR INFORMATION

Corresponding Author

Vikram Vishal − Computational and Experimental Geomechanics Laboratory, Department of Earth Sciences, Indian Institute of Technology (IIT) Bombay, Mumbai 400076, India; National Centre of Excellence in Carbon Capture and Utilization, Indian Institute of Technology (IIT) Bombay, Mumbai 400076, India; ● orcid.org/0000-0002-0896-7844; Phone: +91-22-2576-7254; Email: v.vishal@iitb.ac.in; Fax: +91-22-2576-7253; https://www.geos.iitb.ac.in/index.php/vv/

Authors

Bodhisatwa Hazra − CSIR-Central Institute of Mining and Fuel Research, Dhanbad 826015, India; Academy of Scientific and Innovative Research (AcSIR), Ghaziabad 201002, India; ● orcid.org/0000-0002-3462-7552

Debanjan Chandra − Department of Geoscience and Engineering, Delft University of Technology, 2628 CN Delft, The Netherlands

Sivaji Lahiri − CSIR-Central Institute of Mining and Fuel Research, Dhanbad 826015, India

Chinmay Sethi − CSIR-Central Institute of Mining and Fuel Research, Dhanbad 826015, India; Academy of Scientific and Innovative Research (AcSIR), Ghaziabad 201002, India

Jai Krishna Pandey − CSIR-Central Institute of Mining and Fuel Research, Dhanbad 826015, India; Academy of Scientific and Innovative Research (AcSIR), Ghaziabad 201002, India

Complete contact information is available at:
https://pubs.acs.org/10.1021/acs.energyfuels.3c02320

Notes

The authors declare no competing financial interest.

■ ACKNOWLEDGMENTS

■ REFERENCES

(1) Curtis, J. B. Fractured shale-gas systems. AAPG Bull. 2002, 86, 1921−1938.

(2) Jarvie, D. M.; Hill, R. J.; Ruble, T. E.; Pollastro, R. M. Unconventional shale-gas systems: The Mississippian Barnett Shale of north-central Texas as one model for thermogenic shale-gas assessment. AAPG Bull. 2007, 91, 475−499.

(3) Guo, M.; Lu, X.; Nielsen, C. P.; McElroy, M. B.; Shi, W.; Chen, Y.; Xu, Y. Prospects for shale gas production in China: Implications for water demand. Renewable Sustainable Energy Rev. 2016, 66, 742−750.

(4) Hazra, B.; Wood, D. A.; Vishal, V.; Varma, A. K.; Sakha, D.; Singh, A. K. Porosity controls and fractal disposition of organic-rich Permian shales using low-pressure adsorption techniques. Fuel 2018, 220, 837−848.

(5) Loucks, R. G.; Reed, R. M.; Ruppel, S. C.; Jarvie, D. M. Morphology, genesis, and distribution of nanometer-scale pores in siliceous mudstones of the Mississippian Barnett Shale. J. Sediment. Res. 2009, 79, 848−861.

(6) Loucks, R. G.; Reed, R. M.; Ruppel, S. C.; Hammes, U. Spectrum of pore types and networks in mudrocks and a descriptive classification for matrix-related mudrock pores. AAPG Bull. 2012, 96, 1071−1098.

(7) Ross, D. J.; Bustin, R. M. The importance of shale composition and pore structure upon gas storage potential of shale gas reservoirs. Mar. Pet. Geol. 2009, 26, 916−927.

(8) Milliken, K. L.; Rudnicki, M.; Awwiller, D. N.; Zhang, T. Organic matter−hosted pore system, Marcellus formation (Devonian), Pennsylvania. AAPG Bull. 2013, 97, 177−200.

(9) Mastalerz, M.; Schimmelmann, A.; Drobniak, A.; Chen, Y. Porosity of Devonian and Mississippian New Albany Shale across a maturation gradient: Insights from organic petrology, gas adsorption, and mercury intrusion. AAPG Bull. 2013, 97, 1621−1643.

(10) Labani, M. M.; Rezaee, R.; Saeedi, A.; Al Hinai, A. Evaluation of pore size spectrum of gas shale reservoirs using low pressure

nitrogen adsorption, gas expansion and mercury porosimetry: A case study from the Perth and Canning Basins, Western Australia. *J. Pet. Sci. Eng.* **2013**, *112*, 7−16.

(11) Psarras, P.; Holmes, R.; Vishal, V.; Wilcox, J. Methane and CO2 adsorption capacities of kerogen in the Eagle Ford shale from molecular simulation. *Acc. Chem. Res.* **2017**, *50*, 1818−1828.

(12) Hazra, B.; Wood, D. A.; Vishal, V.; Singh, A. K. Pore characteristics of distinct thermally mature shales: influence of particle size on low-pressure CO2 and N2 adsorption. *Energy Fuels* **2018**, *32*, 8175−8186.

(13) Hazra, B.; Wood, D. A.; Mani, D.; Singh, P. K.; Singh, A. K. *Evaluation of Shale Source Rocks and Reservoirs*; Springer International Publishing: Berlin/Heidelberg, Germany, 2019; Vol. *142*.

(14) Hazra, B.; Vishal, V.; Sethi, C.; Chandra, D. Impact of supercritical CO2 on shale reservoirs and its implication for CO2 sequestration. *Energy Fuels* **2022**, *36*, 9882−9903.

(15) Vishal, V.; Chandra, D.; Bahadur, J.; Sen, D.; Hazra, B.; Mahanta, B.; Mani, D. Interpreting pore dimensions in gas shales using a combination of SEM imaging, small-angle neutron scattering, and low-pressure gas adsorption. *Energy Fuels* **2019**, *33*, 4835−4848.

(16) Chandra, D.; Vishal, V.; Bahadur, J.; Agrawal, A. K.; Das, A.; Hazra, B.; Sen, D. Nano-scale physicochemical attributes and their impact on pore heterogeneity in shale. *Fuel* **2022**, *314*, No. 123070.

(17) Sethi, C.; Hazra, B.; Wood, D. A.; Singh, A. K. Experimental protocols to determine reliable organic geochemistry and geo-mechanical screening criteria for shales. *J. Earth Syst. Sci.* **2023**, *132*, 45.

(18) Sethi, C.; Mastalerz, M.; Hower, J. C.; Hazra, B.; Singh, A. K.; Vishal, V. Using optical-electron correlative microscopy for shales of contrasting thermal maturity. *Int. J. Coal Geol.* **2023**, *274*, No. 104273.

(19) Mastalerz, M.; He, L.; Melnichenko, Y. B.; Rupp, J. A. Porosity of coal and shale: Insights from gas adsorption and SANS/USANS techniques. *Energy Fuels* **2012**, *26*, 5109−5120.

(20) Mastalerz, M.; Hampton, L.; Drobniak, A.; Loope, H. Significance of analytical particle size in low-pressure N2 and CO2 adsorption of coal and shale. *Int. J. Coal Geol.* **2017**, *178*, 122−131.

(21) Chandra, D.; Vishal, V. A critical review on pore to continuum scale imaging techniques for enhanced shale gas recovery. *Earth-Sci. Rev.* **2021**, *217*, No. 103638.

(22) Chandra, D.; Vishal, V.; Debbarma, A.; Banerjee, S.; Pradhan, S. P.; Mishra, M. K. Role of composition and depth on pore attributes of Barakar Formation Gas Shales of Ib Valley, India, using a combination of low-pressure sorption and image analysis. *Energy Fuels* **2020**, *34*, 8085−8098.

(23) Chandra, D.; Vishal, V. A comparison of nano-scale pore attributes of Barakar Formation gas shales from Raniganj and Wardha Basin, India using low pressure sorption and FEG-SEM analysis. *J. Nat. Gas Sci. Eng.* **2020**, *81*, No. 103453.

(24) Chalmers, G. R.; Bustin, R. M.; Power, I. M. Characterization of gas shale pore systems by porosimetry, pycnometry, surface area, and field emission scanning electron microscopy/transmission electron microscopy image analyses: Examples from the Barnett, Woodford, Haynesville, Marcellus, and Doig units. *AAPG Bull.* **2012**, *96*, 1099−1119.

(25) Kuila, U.; Prasad, M. Specific surface area and pore-size distribution in clays and shales. *Geophys. Prospect.* **2013**, *61*, 341−362.

(26) Chen, W.; Zhou, Y.; Yang, L.; Zhao, N.; Lei, Y. Experimental study of low-temperature combustion characteristics of shale rocks. *Combust. Flame* **2018**, *194*, 285−295.

(27) Bai, J.; Kang, Y.; Chen, M.; Liang, L.; You, L.; Li, X. Investigation of multi-gas transport behavior in shales via a pressure pulse method. *Chem. Eng. J.* **2019**, *360*, 1667−1677.

(28) Chandra, D.; Vishal, V.; Bahadur, J.; Sen, D. A novel approach to identify accessible and inaccessible pores in gas shales using combined low-pressure sorption and SAXS/SANS analysis. *Int. J. Coal Geol.* **2020**, *228*, No. 103556.

(29) Chandra, D.; Bakshi, T.; Bahadur, J.; Hazra, B.; Vishal, V.; Kumar, S.; Sen, D.; Singh, T. N. Pore morphology in thermally-treated shales and its implication on CO2 storage applications: A gas

sorption, SEM, and small-angle scattering study. *Fuel* **2023**, *331*, No. 125877.

(30) Vengosh, A.; Warner, N.; Jackson, R.; Darrah, T. The effects of shale gas exploration and hydraulic fracturing on the quality of water resources in the United States. *Procedia Earth Planet. Sci.* **2013**, *7*, 863−866.

(31) Vengosh, A.; Jackson, R. B.; Warner, N.; Darrah, T. H.; Kondash, A. A critical review of the risks to water resources from unconventional shale gas development and hydraulic fracturing in the United States. *Environ. Sci. Technol.* **2014**, *48*, 8334−8348.

(32) Chen, W.; Lei, Y.; Chen, Y.; Sun, J. Pyrolysis and combustion enhance recovery of gas for two China shale rocks. *Energy Fuels* **2016**, *30*, 10298−10305.

(33) Chen, W.; Lei, Y.; Ma, L.; Yang, L. Experimental study of high temperature combustion for enhanced shale gas recovery. *Energy Fuels* **2017**, *31*, 10003−10010.

(34) Chandra, D.; Bakshi, T.; Vishal, V. Thermal effect on pore characteristics of shale under inert and oxic environments: Insights on pore evolution. *Microporous Mesoporous Mater.* **2021**, *316*, No. 110969.

(35) Chapiro, G.; Bruining, J. Combustion enhance recovery of shale gas. *J. Pet. Sci. Eng.* **2015**, *127*, 179−189.

(36) Rigby, S. P.; Jahan, H.; Stevens, L.; Uguna, C.; Snape, C.; Macnaughton, B.; Large, D. J.; Fletcher, R. S. Pore structural evolution of shale following thermochemical treatment. *Mar. Pet. Geol.* **2020**, *112*, No. 104058.

(37) Kang, Z.; Zhao, Y.; Yang, D. Review of oil shale in-situ conversion technology. *Appl. Energy* **2020**, *269*, No. 115121.

(38) Tiwari, P.; Deo, M.; Lin, C. L.; Miller, J. D. Characterization of oil shale pore structure before and after pyrolysis by using X-ray micro CT. *Fuel* **2013**, *107*, 547−554.

(39) Chen, J.; Xiao, X. Evolution of nanoporosity in organic-rich shales during thermal maturation. *Fuel* **2014**, *129*, 173−181.

(40) Sun, L.; Tuo, J.; Zhang, M.; Wu, C.; Wang, Z.; Zheng, Y. Formation and development of the pore structure in Chang 7 member oil-shale from Ordos Basin during organic matter evolution induced by hydrous pyrolysis. *Fuel* **2015**, *158*, 549−557.

(41) Bai, F.; Sun, Y.; Liu, Y.; Guo, M. Evaluation of the porous structure of Huadian oil shale during pyrolysis using multiple approaches. *Fuel* **2017**, *187*, 1−8.

(42) Lei, J.; Pan, B.; Guo, Y.; Fan, Y.; Xue, L.; Deng, S.; Zhang, L.; Ruhan, A. A comprehensive analysis of the pyrolysis effects on oil shale pore structures at multiscale using different measurement methods. *Energy* **2021**, *227*, No. 120359.

(43) Sennoune, M.; Salvador, S.; Quintard, M. Reducing CO2 emissions from oil shale semicoke smoldering combustion by varying the carbonate and fixed carbon contents. *Combust. Flame* **2011**, *158*, 2272−2282.

(44) Hazra, B.; Dutta, S.; Kumar, S. TOC calculation of organic matter rich sediments using Rock-Eval pyrolysis: Critical consideration and insights. *Int. J. Coal Geol.* **2017**, *169*, 106−115.

(45) Hazra, B.; Singh, D. P.; Crosdale, P. J.; Singh, V.; Singh, P. K.; Gangopadhyay, M.; Chakraborty, P. Critical insights from Rock-Eval analysis of vitrains. *Int. J. Coal Geol.* **2021**, *238*, No. 103717.

(46) Hazra, B.; Singh, D. P.; Chakraborty, P.; Singh, P. K.; Sahu, S. G.; Adak, A. K. Using rock-eval S4Tpeak as thermal maturity proxy for shales. *Mar. Pet. Geol.* **2021**, *127*, No. 104977.

(47) Lafargue, E.; Marquis, F.; Pillot, D. Rock-Eval 6 applications in hydrocarbon exploration, production, and soil contamination studies. *Rev. Inst. Fr. Pét.* **1998**, *53*, 421−437.

(48) Behar, F.; Beaumont, V. D. E. B.; Penteado, H. D. B. Rock-Eval 6 technology: performances and developments. *Oil Gas Sci. Technol.* **2001**, *56*, 111−134.

(49) Singh, D. P.; Chandra, D.; Vishal, V.; Hazra, B.; Sarkar, P. Impact of degassing time and temperature on the estimation of pore attributes in shale. *Energy Fuels* **2021**, *35*, 15628−15641.

(50) Behar, F.; Vandenbroucke, M. Chemical modeling of kerogen. *Org. Geochem.* **1987**, *11*, 15.

(51) Hazra, B.; Varma, A. K.; Bandopadhyay, A. K.; Mendhe, V. A.; Singh, B. D.; Saxena, V. K.; Samad, S. K.; Mishra, D. K. Petrographic insights of organic matter conversion of Raniganj basin shales, India. *Int. J. Coal Geol.* **2015**, *150*, 193−209.

(52) Qigui, J.; Yanbin, W.; Jianzhong, Q.; Qin, W.; Caiming, Z. Kinetics of the hydrocarbon generation process of marine source rocks in South China. *Pet. Explor. Dev.* **2010**, *37*, 174−180.

(53) İnan, S.; Henderson, S.; Qathami, S. Oxidation Tmax: a new thermal maturity indicator for hydrocarbon source rocks. *Org. Geochem.* **2017**, *113*, 254−261.

(54) Hazra, B.; Singh, D. P.; Chakraborty, P.; Singh, P. K.; Sahu, S. G.; Adak, A. K. Using rock-eval S4Tpeak as thermal maturity proxy for shales. *Mar. Pet. Geol.* **2021**, *127*, No. 104977.

(55) Rouquerol, J.; Rouquerol, F.; Sing, K. S. W. *Absorption by Powders and Porous Solids*; Academic Press, 1998.

📖 Recommended by ACS

Pore Peak Types and Controlling Factors of Micropores in Different Shale Reservoirs

Shuai Nie, Lei Zhang, *et al.*

AUGUST 30, 2023
ENERGY & FUELS   READ 🗗

Controlling Effect of Shale Pore Connectivity on the Adsorption State of Shale Gas: A Case Study of Continental Shale of Jurassic Ziliujing Formation, Sichuan Basin

Lixun Bai, Lidan Jia, *et al.*

SEPTEMBER 14, 2023
ENERGY & FUELS   READ 🗗

High-Temperature-Induced Pore System Evolution of Immature Shale with Different Total Organic Carbon Contents

Luo Zhuoke, Lingzhi Xie, *et al.*

APRIL 02, 2023
ACS OMEGA   READ 🗗

Pore Structure Characterizations of Shale Oil Reservoirs with Heat Treatment: A Case Study from Dongying Sag, Bohai Bay Basin, China

Pengfei Zhang, Yajie Yin, *et al.*

JULY 16, 2023
ACS OMEGA   READ 🗗

Get More Suggestions >